Temperature-Programmed Desorption of H₂ from Mg-Ni/C for Hydrogen Storage Application

Billy Rudypratama¹, Aditya Eka Nurfitrah², Rizki Ismoyojati², and Bambang Priyono^{1,2,3*}

¹Department of Interdisciplinary Engineering, Faculty of Engineering, Universitas Indonesia, Kampus UI, Depok 16424, Indonesia

* Corresponding author:

tel: +62-81296662815 email: bambang.priyono@ui.ac.id

Received: February 11, 2025 Accepted: July 3, 2025

DOI: 10.22146/ijc.104644

Abstract: Hydrogen is a flexible energy carrier with the potential to replace fossil fuels as a clean and renewable energy source. However, efficient storage systems under ambient conditions are essential for practical applications. This study investigates magnesiumnickel-based metal hydrides for hydrogen storage, enhanced with 20% graphite or additional nickel. The synthesized samples-MgNi2, MgNi2 + graphite 20%, Mg2Ni + graphite 20%, and Mg₂Ni + Ni 1:1—were characterized using XRD, BET, SEM-EDX, and hydrogen temperature-programmed desorption (TPD). Crystallite sizes were found to be 132.125, 137.125, 77.168, and 92.335 nm, respectively. BET analysis revealed surface areas of 2.144, 1.664, 7.113, and 2.308 m²/g, corresponding pore volumes of 0.0038, 0.0031, 0.0137, and 0.0100 cm³/g. TPD results showed that Mg_2Ni + graphite 20% had the fastest desorption rate (46 min), consistent with its highest surface area and pore volume. This sample also achieved the highest hydrogen adsorption capacity at 0.0615 mmol/g. These findings demonstrate that Mg-Ni hydrides, especially those modified with graphite, offer promising performance for hydrogen storage applications, particularly in systems requiring rapid desorption and efficient kinetics, such as fuel-cell electric vehicles. The results highlight the potential of tailored Mg-Ni composites for advanced hydrogen storage solutions.

Keywords: hydrogen storage; metal hydride; magnesium and nickel alloy; chemisorption; hydrogen-temperature-programmed desorption

■ INTRODUCTION

The flexibility of hydrogen as an energy carrier has opened up research opportunities in utilizing hydrogen as an alternative fuel to fossil energy. Hydrogen can be utilized as fuel for industry, transportation, heat production, and power generation to create an environmentally friendly production cycle process [1-4]. In addition to flexibility in utility aspects, hydrogen is easy to produce using various primary energy sources, one of which is by integrating renewable energy with electrolysis technology to produce green hydrogen free from greenhouse gas (GHG) emissions. However, to fully realize the potential of hydrogen, especially in mobile and off-grid applications, the development of efficient and

practical storage systems is crucial. Hydrogen's low volumetric energy density at ambient conditions (0.01 MJ/L) poses a significant challenge for storage, making it essential to explore innovative solutions for safe and compact hydrogen storage [5-6].

Hydrogen can be stored chemically or physically in gas, liquid, or solid phases. Hydrogen storage in the gas phase is carried out by compressing hydrogen at a certain pressure, known as compressed air hydrogen storage (CGH2). The storage system that converts hydrogen into a liquid is called liquefied hydrogen storage (LH2). Those storage methods have drawbacks in terms of storing the hydrogen efficiently. The hydrogen must be compressed into the storage tank to

²Department of Metallurgical and Materials Engineering, Faculty of Engineering, Universitas Indonesia, Kampus UI, Depok 16424, Indonesia

³Tropical Renewable Energy Research Center, Universitas Indonesia, Kampus UI, Depok 16424, Indonesia

maintain its volatility and avoid losses. Thus, CGH2 is not compatible with long-distance mobile hydrogen storage. So does LH2 also need high energy because the hydrogen should be in the cryogenic phase under its boiling point (–253 °C) [7]. In addition to the two commonly used technologies, hydrogen storage technology in solid media uses metal hydride materials, which is quite promising due to its ambient temperature and atmospheric storage conditions [8].

This study aimed to experimentally investigate the hydrogen storage performance of metal hydrides, specifically focusing on Laves-phase intermetallic alloys of the AB₂ and A₂B types. Magnesium (Mg), a lightweight alkaline earth metal with high hydrogen storage potential, was used on the A-site, while nickel (Ni), a transition metal, occupied the B-site, forming MgNi₂ and Mg₂Ni binary alloys [9]. The Mg-Ni system was selected based on its favorable hydrogen storage characteristics, as reported in previous studies [7,10-14], which considered key factors such as performance, cost, and material availability.

To enhance the adsorption and desorption properties, graphite and additional Ni were incorporated into the Mg-Ni system. Graphite acts as a structural stabilizer and dispersant, improving the hydrogen diffusion pathways. Meanwhile, nickel acts as a catalytic agent, improving the dissociation of hydrogen molecules into atomic hydrogen, which is a critical step in the hydrogen adsorption process. This approach followed the work of Sun et al [15]. It aligned with findings by Guo et al. [13], which demonstrated that the addition of carbon and Ni significantly improved the hydrogen storage performance of Mg-Mg₂Ni/C composites. For instance, MgH₂ mixed with these composite materials exhibited a dehydrogenation activation reduced energy 77.6 ± 2.1 kJ/mol, approximately 50% lower than that of MgH_2 (156.3 ± 2.3 kJ/mol). Furthermore, the composite achieved a maximum hydrogen capacity of 6 wt.% at 473 K within 4 min of absorption.

Hydrogen storage performance was evaluated using a chemisorption-based method and hydrogen temperature-programmed desorption (H_2 -TPD). Chemisorption involves the formation of chemical bonds

between the adsorbate and the adsorbent surface, leading to stronger, more stable interactions compared to physisorption [16-18]. Unlike the multilayered nature of physisorption, chemisorption is characterized by monolayer adsorption, terminating once surface saturation is achieved. Due to the strength of the chemical bonds formed, desorption in chemisorption typically requires elevated temperatures (300-400 °C), as governed by the TPD principles. This work presents a novel strategy that combines material modification of the Mg-Ni system with graphite and Ni, alongside comprehensive analysis using chemisorption and H₂-TPD. This approach provided a comprehensive understanding of the synergistic effect of the added materials on the hydrogen adsorption-desorption kinetics and overall storage capacity.

EXPERIMENTAL SECTION

Materials

Mg powder (\geq 98.5%, ~0.1 mm, Sigma-Aldrich) and Ni powder (99.9%, ~150 µm, Sigma-Aldrich) were used as the primary raw materials. In addition, artificial graphite powder (~14.5 nm, Gelon LIB) and extra Ni powder were incorporated as additive materials into the synthesized Mg-Ni alloy. Two types of intermetallic alloys, MgNi₂ and Mg₂Ni, were prepared according to the Mg-Ni phase diagram. A total of four samples were synthesized: two samples of MgNi₂ and two of Mg₂Ni, with each sample having a total mass of 20 g.

Instrumentation

Several tests are conducted to determine the material's physical properties, including X-ray diffraction (XRD), scanning electron microscope-energy dispersive X-ray (SEM-EDX), and surface pore size analyzer through the Brunauer-Emmet-Teller (BET). The phase compositions and crystallographic structures of the synthesized samples were characterized using X-ray diffraction (XRD, PANalytical Empyrean) with Cu K α radiation (λ = 1.5406 Å). Measurements were conducted in the 2 θ range of 20–80°, with a scanning rate of 2°/min, an operating voltage of 40 kV, and a current of 30 mA. Surface area and porosity

characteristics were analyzed by nitrogen adsorption-desorption measurements using the BET method (Quantachrome Quadrasorb-Evo Surface Area and Pore Size Analyzer). Before measurement, the samples were degassed under vacuum at 150 °C for 12 h to remove adsorbed impurities. The specific surface area was calculated from the linear part of the BET plot.

The hydrogen adsorption and desorption behavior was evaluated using H₂-TPD (Autochem II Micrometrics.). The test includes pre-treatment by purging or outgassing at a temperature of 350 °C for 60 min in a helium (He) gas (inert) environment to neutralize the surface from gas contaminants. After the pre-treatment process, the adsorption process is carried out at a room temperature of 40-50 °C with atmospheric pressure for 30 min, followed by purging with argon gas (inert). Then, the process is continued with desorption using the TPD method up to 800 °C with a temperature increase rate of 10 °C/min and a hydrogen gas flow rate of 50 mL/min. The temperature and kinetic rate during desorption can be analyzed using the TPD method through a thermal conductivity detector (TCD) sensor, which is an instrument for detecting the difference in conductivity values of the carrier gas (H₂) expressed in intensity units (a.u.). The peak intensity describes the amount of hydrogen molecule concentration that has been desorbed [19].

Surface morphology and microstructural features were examined using scanning electron microscopy (SEM, JEOL JSM-6510LV). Prior to imaging, the samples were gently ground and dispersed onto carbon tape mounted on an aluminum SEM sample holder. To ensure good conductivity and minimize charging effects during imaging, the samples were coated with a thin layer of gold (Au) using a sputter coater under vacuum conditions. SEM imaging was performed in secondary electron detection mode using an Everhart-Thornley Detector (ETD) at an accelerating voltage (HV) of 30.0 kV. EDS was performed simultaneously to analyze the elemental distribution of Mg, Ni, and C across the sample surfaces. SEM aims to obtain images captured by the instrument to observe the morphology of the micro-sized material structure, while EDX operates on the principle of dispersing light at specific wavelengths, manifested as energy to extract electrons from the innermost layers of the constituent atoms of the material. Then, the extracted electrons provide information related to the weight composition percentage and atomic composition of each element in the material [20].

Procedure

The Mg-Ni alloys were synthesized using a solidstate calcination method. Stoichiometric mixtures of Mg and Ni powders were heated from 25 to 700 °C at a ramp rate of 2 °C/min. The temperature was held at 700 °C for 10 h, approximately 61% below the melting point of 1,147 °C, as indicated in the Mg-Ni phase diagram. Sample preparation was done by weighing and mixing Mg and Ni powders using a mortar. The calcination was conducted under an argon (Ar) atmosphere with a flow rate of 1.5 L/min to prevent oxidation during the reaction. A total of four samples were prepared, consisting of two MgNi₂ and two Mg₂Ni compositions. Both MgNi₂ (Mg = 3.451 g, Ni = 16.549 g) and Mg₂Ni (Mg = 9.198 g, Ni = 10.802 g) samples are synthesized by calcination at 700 °C for 10 h within 20 g of each sample. The molar mass of Mg powder that was used was 24.30 g/mol, while Ni powder was 58.69 g/mol.

Graphite and additional Ni powders were incorporated into selected samples (S2, S3, and S4) via mechanical alloying using a wet ball milling method to enhance surface properties for hydrogen adsorption-desorption. Sample S1 was retained as pure MgNi₂ for comparison. The doping compositions were as follows: S2—20 wt.% graphite (4 g), S3—50 wt.% Ni (10 g), and S4—20 wt.% graphite (4 g), as summarized in Table 1.

Ball milling was performed for 120 min at 240 rpm using a planetary mill with a stainless-steel vial and zirconia balls, with a material-to-ball ratio of 1:3 and 12 mL of ethanol as the process medium, based on the procedure by Joseph et al. [21]. Ethanol acted as a dispersion medium and prevented excessive agglomeration or structural degradation. The resulting slurry was dried in an oven at 80 °C for 4 h and then stored in a dry box.

San	nple ID	Base alloy	Doping material	*Doping composition (wt.%)	Doping mass (g)	Total mass (g)			
	S1	$MgNi_2$				20			
	S2	$MgNi_2$	Graphite (C)	20	4	20			
	S3	Mg_2Ni	Nickel (Ni)	50	10	20			
	S4	Mg_2Ni	Graphite (C)	20	4	20			

Table 1. Composition of synthesized Mg-Ni-based samples with doping variations

^{*}Doping composition refers to the additive's weight percent to the total weight of the sample

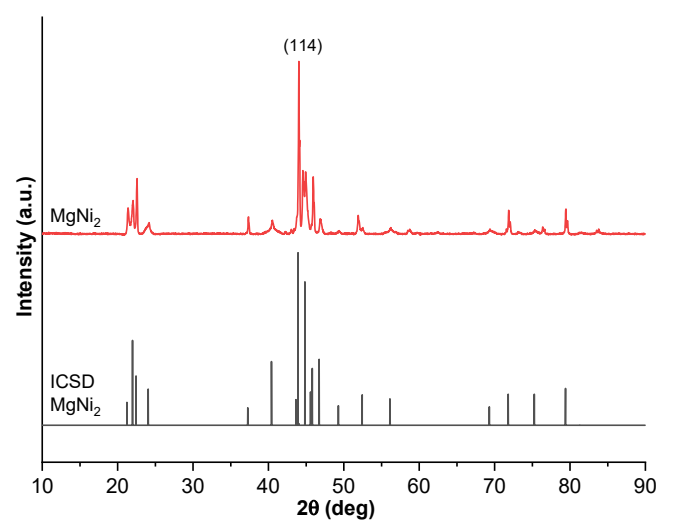


Fig 1. XRD pattern of MgNi $_2$ compared to ICSD: #98-010-4838

RESULTS AND DISCUSSION

XRD Result and Analysis on MgNi₂ and Mg₂Ni Alloys

The MgNi₂ has been determined by the peak of intensity at a certain 2θ , as shown in Fig. 1. To ensure accurate phase identification, the XRD patterns were analyzed using HighScore Plus with manual adjustment of peak positions, fitting range, and background correction. The test results determine the material's lattice parameters through the X-ray spectrum's intensity peaks. To observe the results of the light reflection, the Bragg's Law principle [22]. In addition to the lattice parameters of the crystal structure, the crystallite size is also obtained through the Debye-Scherrer equation [23]. Goodness of fit (GoF) and Fit Score values were carefully validated against ICSD reference data. Those peak positions have been fitted and matched based on the Inorganic Crystal Structure Database (ICSD). The ICSD data reference for the binary alloy MgNi₂ is ICSD #98-010-4838. A fit score of 79 and a GoF of 1.86 were obtained, where the GoF has met the fit standards, namely < 10 and lies between 1-2 [24]. Crystallography analysis was conducted to obtain the lattice parameters of the crystal structure, where the crystal is hexagonal in shape with a value of 0.482 nm, b value of 0.482 nm, and c value of 1.583 nm, as well as a cell volume of 0.319 nm³. The intensity peak is located at 2θ of 44.024° with the plane positions h, k, and l of (114). The analysis of crystallite size was conducted only at the highest peak with an FWHM value of 0.093°, resulting in a crystallite size of 132.125 nm.

Then, MgNi₂ and Mg₂Ni with the additional of graphite 20 wt.% was analyzed to observe the effect of additional graphite on the changes in the crystal structure of the alloy is shown in Fig. 2. Fig. 2(a) shown in the ICSD data references for the MgNi₂ + graphite 20% sample use two references for each MgNi₂ and graphite phase, which are ICSD: #98-010-4838 and ICSD: #98-005-2230. A fit score of 74 for ICSD MgNi₂ and 47 for ICSD graphite was obtained with the GoF value of 1.278. Fig. 2(b) shows that the ICSD data for the Mg₂Ni + Ni 1:1 sample uses two references for each Mg₂Ni and Ni phase, namely ICSD #98-003-0713 and ICSD #98-005-2231. A fitting score 67 was obtained for ICSD Mg₂Ni and 30 for ICSD graphite, with the value of GoF is 1.360.

Crystallographic analysis can be seen in Table 2. Crystallography analysis was conducted where the crystal is hexagonal with a value of 0.483 nm, b value of 0.483 nm, and c value of 1.572 nm, the cell volume is 0.318 nm³, and an intensity peak located at 20 43.936° with the plane positions h, k, and l (114) in the MgNi₂ phase. Meanwhile, the graphite phase is also hexagonal with a value of 0.245 nm, b value of 0.245 nm, c value of 0.667 nm, the cell volume is 0.035 nm³, and the highest intensity peak is located at 20 26.575° with the plane positions h, k, and l (002). The cell volume in the MgNi₂ phase after the addition of graphite decreased by 0.001 nm³. The crystallite size of the MgNi₂ phase after

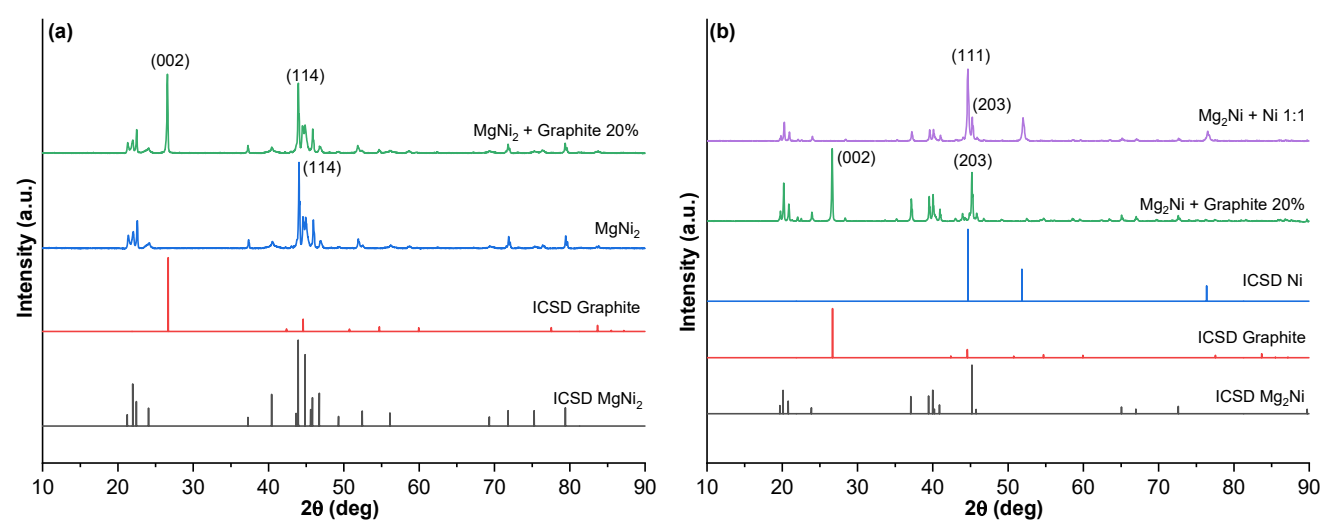


Fig 2. XRD pattern of (a) MgNi₂ and MgNi₂ + graphite 20%, and (b) Mg₂Ni + graphite 20% and Mg₂Ni + Ni 1:1

Table 2. Comparison of lattice parameters and crystallite size between MgNi₂ and MgNi₂ + graphite 20 wt.%

Sample	h-k-l	a (nm)	<i>b</i> (nm)	c (nm)	Cell volume (nm³)	Crystallite size (nm)
MgNi ₂	(114)	0.482	0.482	1.583	0.319	132.125
MgNi ₂ + graphite 20%	(114)	0.483	0.483	1.572	0.318	137.125
Mg ₂ Ni + graphite 20%	(203)	0.521	0.521	1.323	0.310	77.168
$Mg_2Ni + Ni 1:1$	(203)	0.520	0.520	1.322	0.310	92.335

the addition of graphite was determined only at the highest peak with an FWHM value of 0.116° , resulting in a crystallite size of 137.125 nm. Mg₂Ni crystal is hexagonal with a value of 0.520 nm, b value of 0.520 nm, and c value of 1.322 nm, a cell volume of 0.310 nm³, and the intensity peak located at 20 45.361° with the plane positions h, k, and l (203). The structure form of Ni phase is cubic with a, b, and c values of 0.352 nm, a cell volume of 0.043 nm³, and the highest intensity peak located at 20 44.752° with the plane positions h, k, and l (111). The cell volume values did not change in both samples, Mg₂Ni + graphite 20% and Mg₂Ni + Ni 1:1.

The crystallite size results of the Mg_2Ni phase after the addition of Ni were conducted only at the highest peak with an FWHM value of 0.114° , resulting in a crystallite size of 92.335 nm. The mechanical alloying process via ball milling can induce lattice strain and reduce crystallite size, which may lead to slight distortions in lattice parameters. This effect is attributed to structural imperfections introduced during the high-energy milling process. The results of the crystallite size change after the additional doping of Ni on Mg_2Ni , where the crystallite

size in the Mg₂Ni + Ni 1:1 is larger than the Mg₂Ni + graphite 20%, with an increase of 19.6%. However, the crystallite size in both Mg2Ni samples after mixing with the two different materials remains smaller than the crystallite size in both MgNi₂ samples. Crystallography analysis was conducted where the crystal is hexagonal with a value of 0.483 nm, b value of 0.483 nm, and c value of 1.572 nm, the cell volume is 0.318 nm³, and an intensity peak located at 20 43.936° with the plane positions h, k, and l (114) in the MgNi₂ phase. Meanwhile, the graphite phase is also hexagonal with a value of 0.245 nm, b value of 0.245 nm, c value of 0.667 nm, the cell volume is 0.035 nm³, and the highest intensity peak is located at 20 26.575° with the plane positions h, k, and l (002). The cell volume in the MgNi₂ phase after the addition of graphite decreased by 0.001 nm³. The crystallite size of the MgNi₂ phase after the addition of graphite was determined only at the highest peak with an FWHM value of 0.116° , resulting in a crystallite size of 137.125 nm.

There are two types of Mg₂Ni materials with different additional doping materials: Mg₂Ni + graphite

20% and Mg₂Ni + Ni with 50 wt.% of Ni powder to the total weight. ICSD data references for the Mg2Ni + graphite 20% use two references for each Mg2Ni and graphite phase: ICSD #98-003-0713 and ICSD #98-005-2230. A fit score of 87 for ICSD Mg2Ni and 37 for ICSD graphite was obtained, and the GoF value is 1.053. Crystallography analysis was conducted where the Mg₂Ni crystal is hexagonal with a value of 0.521 nm, b value of 0.521 nm, and c value of 1.323 nm, a cell volume of 0.310 nm³, and the intensity peak located at 2θ 45.298° with the plane positions h, k, and l (203) in the Mg₂Ni phase. The graphite phase is also hexagonal with a value of 0.246 nm, b value of 0.246 nm, c value of 0.670 nm, a cell volume of 0.035 nm³, and the highest intensity peak located at 2θ 26.674° with the plane positions h, k, and l. (002). The difference in the stoichiometry of the mixed materials Mg and Ni between MgNi2 and Mg2Ni with the same mixed material—which is graphite at 20 wt.% of the total weight-affects the cell volume with a difference of 0.008 nm³, where the cell volume in the MgNi₂ phase is larger than in the Mg₂Ni phase. The crystallite size of the Mg₂Ni phase after adding graphite was determined only at the highest peak within the FWHM value of 0.127°, resulting in a crystallite size of 77.168 nm. The results indicate that the crystallite size changes with the different stoichiometry of MgNi2 and Mg2Ni, with the crystallite size in the MgNi₂ phase being larger than that in the Mg2Ni phase. The results of the plotted sample peak points of the Mg₂Ni + graphite 20% can be seen in Fig. 3.

Surface Area and Pore Size Results on Alloys

The first sample to be discussed is the MgNi₂ in Fig. 4(a), using N₂— which is then referred to as the adsorbate —and adsorption is carried out under STP conditions. The desorption process of N₂ was carried out at 300 °C for 4 h, as shown in Fig. 4. The results of this test are the total pore volume, the surface area of the metal, and the average pore radius [25]. The isothermal adsorption curve of the MgNi₂ sample falls into type III, which is interpreted as a non-porous material, possibly macroporous with relatively low energy adsorption [26]. The total pore volume of the MgNi₂ is 0.0038 cm³/g, with the surface area was obtained at 2.144 m²/g and an average pore

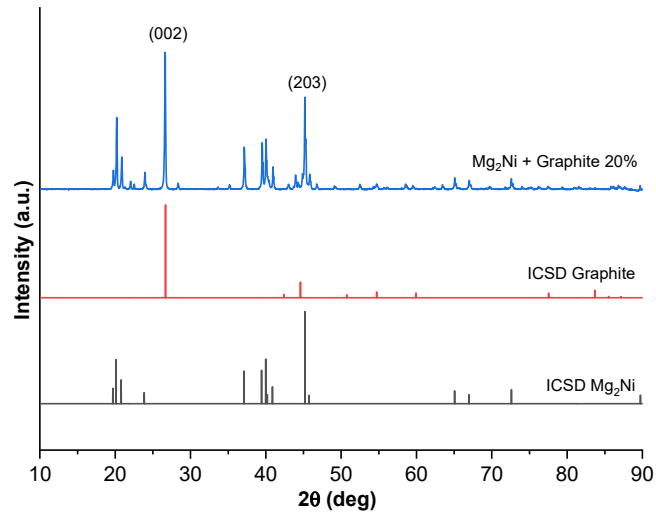
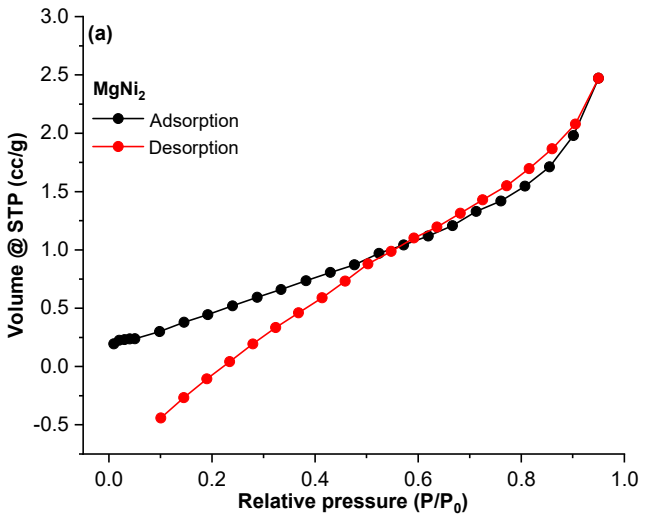
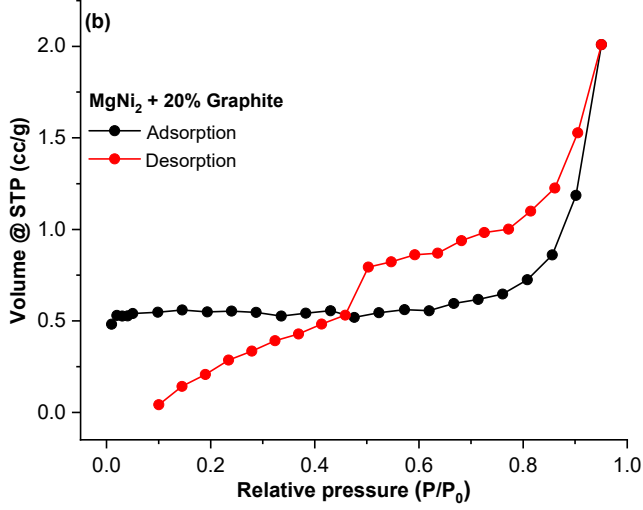


Fig 1. XRD pattern of Mg_2Ni + graphite 20% compared to ICSD #98-003-0713 and 98-005-2230





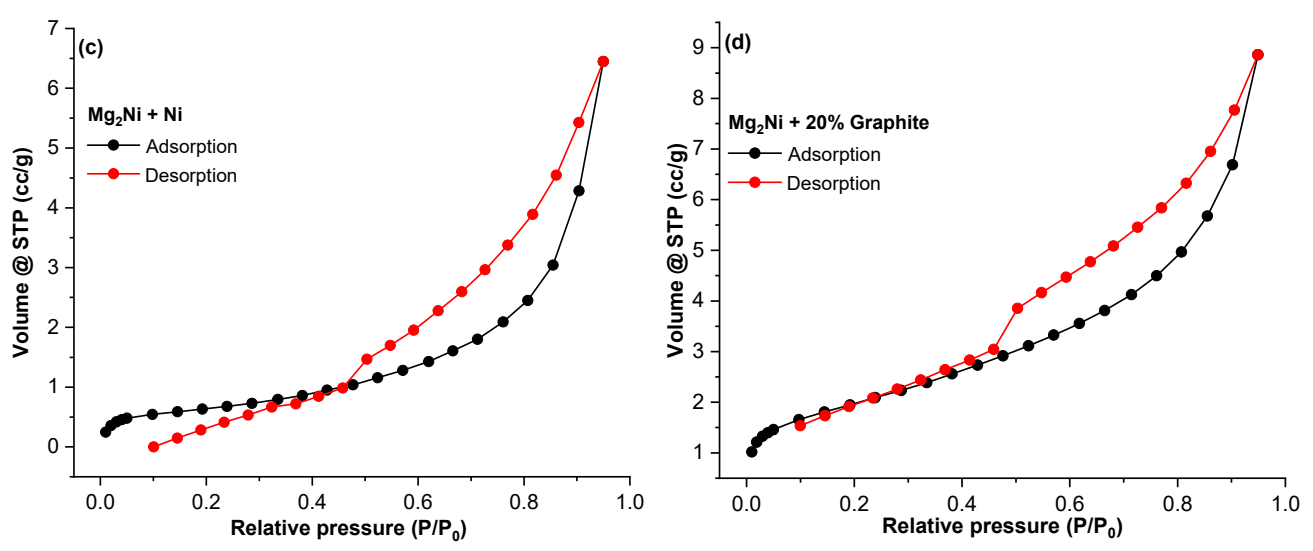


Fig 4. N₂ isothermal adsorption curve of MgNi₂ and Mg₂Ni samples

radius of 3.566 nm. The MgNi₂ sample, after the addition of 20 wt.% graphite, was analyzed to observe the effect of graphite addition on the metal mixture. The isotherm adsorption curve for the MgNi₂ + graphite 20% sample falls into type II, which is interpreted as a non-porous material, possibly macroporous, and has relatively high energy adsorption capacity [26]. The total pore volume in the MgNi₂ + 20% Graphite sample is 0.0031 cm³/g, where the pore volume is smaller than that of the sample before graphite was added. The surface area of the MgNi₂ + graphite 20% is 1.664 m²/g with an average pore radius of 3.737 nm.

The test on the following two different types of samples was conducted to determine the effect of the differing composition of the Mg and Ni mixtures on the material's pore volume and surface area. The isotherm adsorption curve of the Mg₂Ni + Ni 1:1 falls into type II, which has the same interpretation as the MgNi₂ + graphite 20% in Fig. 4(b) and 4(c). The total pore volume in the Mg₂Ni + Ni 1:1 sample is 0.0100 cm³/g, where the pore volume in this sample is larger than both previous samples of MgNi₂. The surface area of the Mg₂Ni + Ni 1:1 is 2.308 m²/g with an average pore radius of 8.644 nm. The increase in pore volume and surface area of the material is related to the crystallite size from the XRD analysis results. The crystallite size in the Mg₂Ni + Ni 1:1 sample is smaller compared to both MgNi2 samples, indicating that the smaller the crystallite size of the material, the greater the surface contact area during the adsorption process [19].

The Mg₂Ni + graphite 20% was tested to observe the effect of graphite addition on the Mg2Ni metal mixture in Fig. 4(d). The shape of the isotherm adsorption curve for the Mg₂Ni + 20% graphite sample falls into type II. The total pore volume for the Mg₂Ni + graphite 20% sample is 0.0137 cm³/g, where the pore volume in this sample is larger than in the three previous samples. The surface area value of the Mg₂Ni + graphite 20% is 7.113 m²/g with an average pore radius of 3.853 nm. This result is in line with the XRD analysis results, where the Mg₂Ni + graphite 20% has the smallest crystallite size compared to the other three samples. Although the BET analysis shows open-loop isotherms in Fig. 4(a-c), this could be attributed to the presence of macroporous structures or incomplete desorption cycles. Such behavior has also been reported in studies involving Mg-based alloys with low surface areas, where the interaction between adsorbate and surface is weak, leading to non-ideal isotherm closure. The surface area and pore size analysis results for the four samples are listed in Table 3.

SEM-EDX Results on the Morphology Structure of Alloys

The structure of the $MgNi_2$ sample changes its crystal shape after adding graphite material. It increases

		1 1	
Sample	Total pore volume (cm³/g)	Surface area (m²/g)	Average pore radius (nm)
MgNi ₂	0.0038	2.144	3.566
MgNi ₂ + graphite 20%	0.0031	1.664	3.737
$Mg_2Ni + Ni 1:1$	0.0100	2.308	8.644
Mg ₂ Ni + graphite 20%	0.0137	7.113	3.853

Table 3. BET surface area and pore size comparison

in particle size but is not significant when observed at $10,000 \times$ magnification. This result is related to the results of the crystal size analysis, where the MgNi₂ + 20% Graphite sample is larger than MgNi₂ without the addition of graphite because the crystal structure is a constituent element of grains or particles. Regarding the material's morphological structure, the crystal shape in the MgNi₂ + graphite is 20% more distinct than the crystal shape in the MgNi₂. The morphological images of both MgNi₂ samples are shown in Fig. 5.

The results of both Mg_2Ni samples with Ni and Mg_2Ni with graphite show no difference in structural form, where both samples have the same structural morphology at a magnification of $10,000\times$. In terms of

particle size, the Mg₂Ni + graphite 20% sample has a larger particle size compared to the Mg₂Ni + Ni 1:1 sample. Although SEM images provide visual information about particle morphology and size, these particles often consist of agglomerates of smaller crystallites. It should be noted that the particle size observed in SEM refers to agglomerates or grains. In contrast, the crystallite size obtained from XRD reflects the coherent diffraction domains, which are typically much smaller. The crystal structure of the samples became distinct after adding material to both the MgNi₂ and Mg₂Ni samples. The morphology images of the Mg₂Ni + Ni 1:1 and Mg₂Ni + graphite 20% samples are shown in Fig. 6.

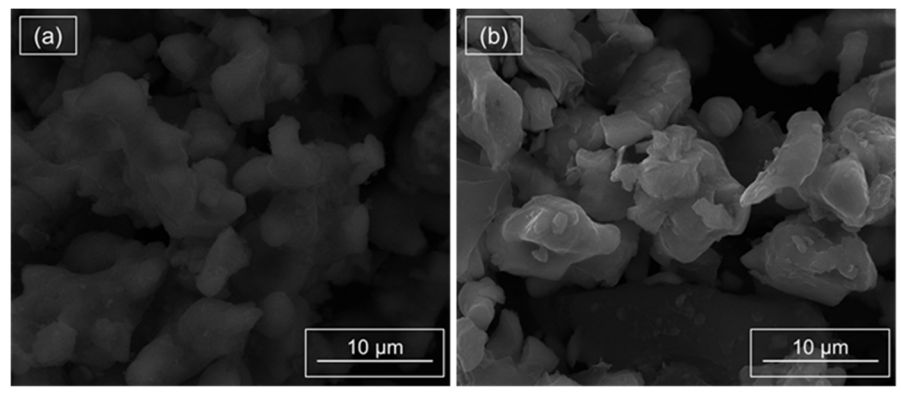


Fig 5. SEM results on (a) MgNi₂ and (b) MgNi₂ + graphite 20%

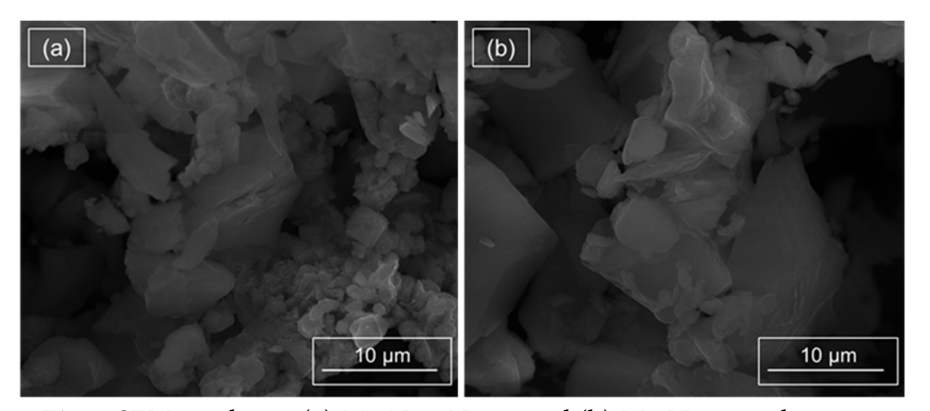


Fig 6. SEM results on (a) Mg₂Ni + Ni 1:1 and (b) Mg₂Ni + graphite 20%

Sample	Spot	%Weight			%Atomic		
Sample		Mg	Ni	С	Mg	Ni	С
MaNi	1	25.53	68.60	1.51	40.24	44.77	4.82
$MgNi_2$	2	27.22	67.07	1.13	42.71	43.59	3.59
MaNi graphita 200/	1	19.81	59.52	16.09	23.58	29.35	38.78
MgNi ₂ + graphite 20%	2	15.61	65.67	16.76	19.56	34.02	42.51
Ma Ni + Ni 1.1	1	37.57	57.47	1.36	54.15	34.30	3.97
$Mg_2Ni + Ni 1:1$	2	40.47	52.04	2.49	54.21	28.87	6.75
Ma Ni Lamanhita 200/	1	24.94	48.79	19.73	26.48	21.45	42.39
Mg ₂ Ni + graphite 20%	2	33.06	48.27	14.73	37.29	22.54	33.62

Table 4. Weight and atomic percentage of each element

The weight and atomic percentage of the constituent elements of the material from the EDX results were plotted. This was conducted at two spots for each sample, covering weight and atomic percentages. All spots have been shown on 10,000× magnification, and these samples have been reviewed in different spots. The weight and atomic percentage of each element have been listed in Table 4. The EDX results show that the increase in weight and atomic percentages is consistent with the samples made. The spread of the mixture is good enough, as it is shown that the increase follows the increase of the additional material in their weight and atomic percentage.

Adsorption and Desorption Performance Test Result

The total hydrogen absorbed into the surface of the $MgNi_2$ sample is 0.0029 mmol with a sample weight of 0.0527 g, so the total hydrogen absorbed on the material's surface per unit weight of the sample is 0.0550 mmol/g. The desorption process is carried out with the endothermic principle from the condition of the hydrogen-saturated sample until the sample's pores are empty, marked by a stable TCD intensity value. The TPD graph for the $MgNi_2$ sample is shown in Fig. 7.

From the H₂-TPD graph is known that the hydrogen desorption process in the MgNi₂ (Fig. 7(a)) sample starts to become active at a temperature of 300 °C and continues to increase until it stabilizes at a temperature of 800 °C with a duration of 100 min, indicating that hydrogen molecules have desorbed from the surface of the material. The total hydrogen absorbed into the surface of the MgNi₂ + graphite 20% with a sample weight of 0.0504 g is 0.0031 mmol, resulting in total hydrogen absorbed on the

material's surface per sample weight of 0.0615 mmol/g. This result shows that the hydrogen adsorption capacity on the MgNi₂ + graphite 20% sample increased compared to the MgNi₂ without the addition of graphite. This result is related to the result of surface area and pore analysis, where the pore radius of the MgNi2 surface increased after the addition of graphite. Thus, the contact area on the surface is enlarging, and the material's adsorption capacity is enhanced [13]. The result of the desorption process from the H2-TPD graph (Fig. 7(b)) shows that the hydrogen desorption process in the MgNi₂ + graphite 20% starts to become active at a temperature of 300 °C and continues to increase until it stabilizes at a temperature of 550 °C with a duration of 52 min. This indicates that the hydrogen molecules have been fully desorbed from the material's surface in less time than the MgNi₂ without adding graphite.

The total hydrogen adsorbed into the surface of the $Mg_2Ni + Ni$ 1:1 with a sample weight of 0.0574 g is 0.0035 mmol (Fig. 7(c)); thus, the total hydrogen adsorbed on the material's surface per sample weight is 0.0610 mmol/g. These results indicate that the hydrogen adsorption capacity on the surface of the Mg_2Ni sample is greater compared to the $MgNi_2$ sample. Meanwhile, in the desorption results through the H_2 -TPD graph, it is known that the $Mg_2Ni + Ni$ 1:1 sample starts to become active at a temperature of 300 °C and continues to increase until it declined and stabilizes at a temperature of 650 °C with a duration of 62 min, indicating that the hydrogen molecules have been completely desorbed from the material's surface. The results of the adsorption test on the material $Mg_2Ni + graphite$ 20% yielded a total

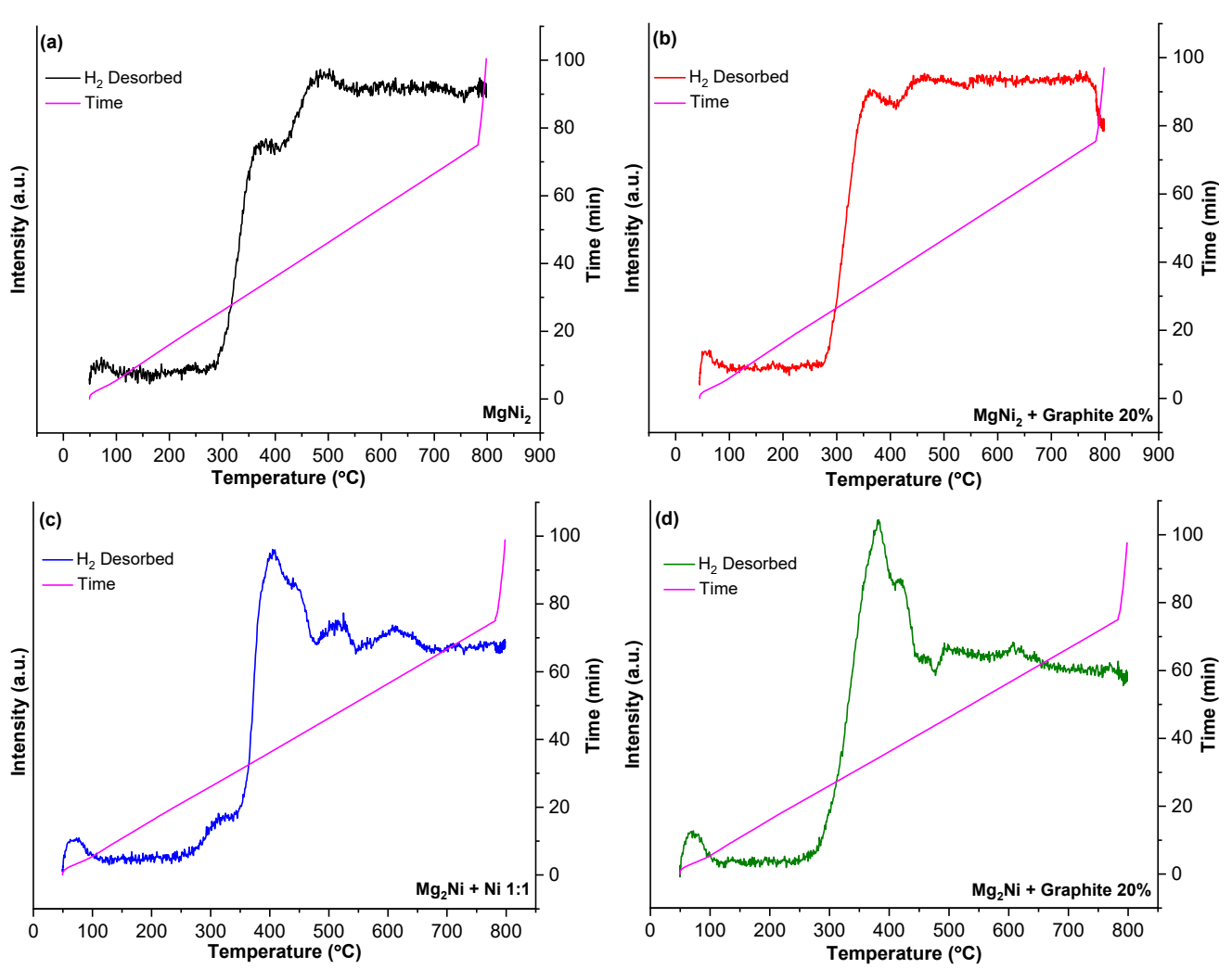


Fig 7. Desorption process through TPD: (a) MgNi₂, (b) MgNi₂ + graphite 20%, (c) Mg₂Ni + Ni 1:1, and (d) Mg₂Ni + graphite 20%

of hydrogen molecules adsorbed into the material's surface, with a sample weight of 0.0553 g corresponding to 0.0033 mmol, resulting in a total hydrogen adsorption per sample weight of 0.0600 mmol/g. The adsorption test results show that the total hydrogen adsorbed on the surface of the Mg₂Ni + graphite 20% sample is greater compared to MgNi₂, where based on the pore radius of the Mg₂Ni + graphite 20% sample is larger than that of MgNi₂ resulting in a larger surface contact area and a higher ability to adsorb hydrogen. However, the hydrogen adsorption capacity of the Mg₂Ni + graphite 20% sample is similar to that of the MgNi₂ + graphite 20% sample, even though the Mg₂Ni + graphite 20% sample has a larger pore radius. This may be caused by several factors,

including the environmental conditions and equipment during the testing, the different room temperatures during the testing, or the treatment during pretreatment or purging, resulting in contaminants still present in the sample. The desorption results through the H₂-TPD (Fig. 7(d)) graph show that the Mg₂Ni + graphite 20% sample starts to become active at 300 °C and continues to increase until it declines and stabilizes at 500 °C with a duration of 46 min. This indicates that hydrogen molecules have been fully desorbed from the material's surface in less time than the previous three samples. In hydrogen storage applications, a faster desorption rate is generally preferred as it enables rapid hydrogen release when needed, which is critical for

practical use, particularly in energy applications such as fuel cells, portable devices, or transportation systems [27].

CONCLUSION

The XRD test results show that the four samples have forming phases corresponding to the materials' names: MgNi₂, MgNi₂ + graphite 20%, Mg₂Ni + graphite 20%, and Mg₂Ni + Ni 1:1, with crystallite sizes of 132.125, 137.125, 77.168, and 92.335 nm, respectively. The surface and pore analysis results show that MgNi₂ + graphite 20% has the smallest surface area and pore volume compared to other samples, while Mg2Ni + graphite 20% has the largest surface area and pore volume. The SEM results show the morphological structure of each sample, where all samples with added material have a more distinct crystalline structure. Meanwhile, the structural shape of the MgNi2 is not clearly visible. In the EDX result, the distribution of the material's constituent elements is evenly spread and tends to align with the composition of the material made according to the weight percentage and atomic percentage. The highest hydrogen adsorption capacity was found in the MgNi₂ + graphite 20% material at 0.0615 mmol/g, while the lowest was in the MgNi₂ material at 0.0550 mmol/g. Then, the results from TPD show a correlation with the analysis of pore volume and surface area where the MgNi₂ + graphite 20% material which has the largest surface area and pore volume —also has the fastest desorption kinetic rate (46 min) and the lowest temperature compared to other samples to completely release hydrogen from the material surface (300-500 °C). A faster desorption rate ensures quick hydrogen release when it's needed, especially in applications like vehicles or portable power systems. In fuel-cell electric vehicles (FCEVs), faster hydrogen desorption from the storage material enables quicker fuel cell activation and shorter refueling times. Consequently, this enhances the system's responsiveness and improves the overall power output performance of the FCEVs.

ACKNOWLEDGMENTS

We gratefully acknowledge the financial support of the Ministry of Education, Culture, Research, and Technology of the Republic of Indonesia through *Hibah* Publikasi Terindeks Internasional (PUTI) Pascasarjana (contract number NKB-118/UN2.RST/HKP.05.00/2024).

CONFLICT OF INTEREST

All authors declare that we have no conflict of interest or financial conflict to disclose.

AUTHOR CONTRIBUTIONS

Billy Rudypratama: Writing – original draft, data curation, conceptualization, investigation, methodology, resources; Aditya Eka Nurfitrah: Review & editing, technical lab. operation, validation; Rizki Ismoyojati: Review & editing, technical lab. operation, validation; Bambang Priyono: Supervision, validation, review & editing, conceptualization.

■ REFERENCES

- [1] Tashie-Lewis, B.C., and Nnabuife, S.G., 2021, Hydrogen production, distribution, storage and power conversion in a hydrogen economy A technology review, *Chem. Eng. J. Adv.*, 8, 100172.
- [2] Wang, T., Cao, X., and Jiao, L., 2022, PEM water electrolysis for hydrogen production: Fundamentals, advances, and prospects, *Carbon Neutrality*, 1 (1), 21.
- [3] Shin, H., Jang, D., Lee, S., Cho, H.S., Kim, K.H., and Kang, S., 2023, Techno-economic evaluation of green hydrogen production with low-temperature water electrolysis technologies directly coupled with renewable power sources, *Energy Convers. Manage.*, 286, 117083.
- [4] Achour, Y., Berrada, A., Arechkik, A., and El Mrabet, R., 2023, Techno-economic assessment of hydrogen production from three different solar photovoltaic technologies, *Int. J. Hydrogen Energy*, 48 (83), 32261–32276.
- [5] Yang, M., Hunger, R., Berrettoni, S., Sprecher, B., and Wang, B., 2023, A review of hydrogen storage and transport technologies, *Clean Energy*, 7 (1), 190–216.
- [6] Kim, D.W., Jung, M., Shin, D.Y., Kim, N., Park, J., Lee, J.H., Oh, H., and Hong, C.S., 2024, Fine-tuned MOF-74 type variants with open metal sites for high volumetric hydrogen storage at near-ambient temperature, *Chem. Eng. J.*, 489, 151500.

- [7] Klopčič, N., Grimmer, I., Winkler, F., Sartory, M., and Trattner, A., 2023, A review on metal hydride materials for hydrogen storage, *J. Energy Storage*, 72, 108456.
- [8] Danebergs, J., and Deledda, S., 2024, Can hydrogen storage in metal hydrides be economically competitive with compressed and liquid hydrogen storage? A techno-economical perspective for the maritime sector, *Int. J. Hydrogen Energy*, 50, 1040–1054.
- [9] Yartys, V.A., and Lototskyy, M.V., 2022, Laves type intermetallic compounds as hydrogen storage materials: A review, *J. Alloys Compd.*, 916, 165219.
- [10] Bellosta von Colbe, J., Ares, J.R., Barale, J., Baricco, M., Buckley, C., Capurso, G., Gallandat, N., Grant, D.M., Guzik, M.N., Jacob, I., Jensen, E.H., Jensen, T., Jepsen, J., Klassen, T., Lototskyy, M.V., Manickam, K., Montone, A., Puszkiel, J., Sartori, S., Sheppard, D.A., Stuart, A., Walker, G., Webb, C.J., Yang, H., Yartys, V., Züttel, A., and Dornheim, M., 2019, Application of hydrides in hydrogen storage and compression: Achievements, outlook and perspectives, *Int. J. Hydrogen Energy*, 44 (15), 7780–7808.
- [11] Guerrero-Ortiz, R., Tena-García, J.R., Flores-Jacobo, A., and Suárez-Alcántara, K., 2019, From the can to the tank: NaAlH₄ from recycled aluminum, *Int. J. Hydrogen Energy*, 44 (36), 20183–20190.
- [12] Ding, Z., Li, S., Zhou, Y., Chen, Z., Yang, W., Ma, W., and Shaw, L., 2020, LiBH₄ for hydrogen storage New perspectives, *Nano Mater. Sci.*, 2 (2), 109–119.
- [13] Guo, S., Yu, Z., Li, Y., Fu, Y., Zhang, Z., and Han, S., 2024, Preparation of Mg-Mg₂Ni/C composite and its excellent hydrogen storage properties, *J. Alloys Compd.*, 976, 173035.
- [14] Zhang, B., Zeng, Z., Li, J., Guo, X., Xia, C., and Yang, T., 2024, Microstructure and hydrogen storage properties of magnesium–gallium binary alloys, *J. Phys. Chem. Solids*, 190, 112028.
- [15] Sun, L., Yao, P., Liu, H., Bradhurst, D.H., and Dou, S., 1999, Mg₂Ni hydride electrodes prepared by sintering and subsequent ball milling with Ni powders, *J. Alloys Compd.*, 293-295, 536–540.
- [16] Atif, M., Haider, H.Z., Bongiovanni, R., Fayyaz, M., Razzaq, T., and Gul, S., 2022, Physisorption and

- chemisorption trends in surface modification of carbon black, *Surf. Interfaces*, 31, 102080.
- [17] Cataldo, F., 2020, On the characterisation of carbon black from tire pyrolysis, *Fullerenes, Nanotubes Carbon Nanostruct.*, 28 (5), 368–376.
- [18] Yang, W.H., Kim, M.H., and Ham, S.W., 2007, Effect of calcination temperature on the low-temperature oxidation of CO over CoO_x/TiO₂ catalysts, *Catal. Today*, 123 (1-4), 94–103.
- [19] Fu, Y., Ding, Z., Zhang, L., Zhang, H., Wang, W., Li, Y., and Han, S., 2021, Catalytic effect of a novel MgC_{0.5}Co₃ compound on the dehydrogenation of MgH₂, *Prog. Nat. Sci.: Mater. Int.*, 31 (2), 264–269.
- [20] Mahdi, M.A., Oroumi, G., Samimi, F., Dawi, E.A., Abed, M.J., Alzaidy, A.H., Jasim, L.S., and Salavati-Niasari, M., 2024, Tailoring the innovative Lu₂CrMnO₆ double perovskite nanostructure as an efficient electrode materials for electrochemical hydrogen storage application, *J. Energy Storage*, 88, 111660.
- [21] Joseph, B., Schiavo, B., D'Al Staiti, G., and Sekhar, B.R., 2011, An experimental investigation on the poor hydrogen sorption properties of nanostructured LaNi₅ prepared by ball-milling, *Int. J. Hydrogen Energy*, 36 (13), 7914–7919.
- [22] Holm, T., 2012, Synthesis and characterisation of the nanostructured magnesium-lanthanum-nickel alloys for Ni-metal hydride battery applications, *Thesis*, Department of Materials Science and Engineering, Faculty of Natural Sciences and Technology, NTNU, Trondheim, Norway.
- [23] Sivagami, M., and Asharani, I.V., 2022, Phytomediated Ni/NiO NPs and their catalytic applications-A short review, *Inorg. Chem. Commun.*, 145, 110054.
- [24] Alaih, A.F.F., Triyono, D., Dwiputra, M.A., and Nugroho, F.A.A., 2024, Ultrafast and low-hysteresis humidity sensors based on mesoporous LaFe_{0.925}Ti_{0.075}O₃ perovskite, *Sens. Actuators*, *B*, 412, 135810.
- [25] Nuriskasari, I., Syahrial, A.Z., Ivandini, T.A., Sumboja, A., Priyono, B., Yan, Q., Destyorini, F., and Priyono, S., 2024, Synthesis of graphitic carbon from

- empty palm oil fruit bunches through single-step graphitization process using K₂FeO₄-KOH catalyst as lithium ion battery anode, *Results Eng.*, 24, 103273.
- [26] Condon, J.B., 2006, Surface Area and Porosity Determinations by Physisorption: Measurements and
- Theory, Elsevier, Amsterdam, Netherlands.
- [27] Abbasian Hamedani, E., Alenabi, S.A., and Talebi, S., 2024, Hydrogen as an energy source: A review of production technologies and challenges of fuel cell vehicles, *Energy Rep.*, 12, 3778–3794.